Experimental qudit state estimation via point tomography

D. Martínez,[1,2,3] L. Pereira,[4] K. Sawada,[1,2] P. González,[1,2] J. Cariñe,[5] M. Muñoz,[6] A. Delgado,[1,2] E. S. Gómez,[1] S. P. Walborn,[1,2] and G. Lima[1,2,*]

[1]*Departamento de Física, Universidad de Concepción, 160-C Concepción, Chile*

[2]*Millennium Institute for Research in Optics, Universidad de Concepción, 160-C Concepción, Chile*

[3]*Vienna Center for Quantum Science and Technology (VCQ) and Christian Doppler Laboratory for Photonic Quantum Computer, Faculty of Physics, University of Vienna, 1090 Vienna, Austria*

[4]*ICFO—Institut de Ciencies Fotoniques, The Barcelona Institute of Science and Technology, 08860 Castelldefels, Barcelona, Spain*

[5]*Departamento de Ingeniería Eléctrica, Universidad Católica de la Santísima Concepción, Concepción, Chile*

[6]*Fundação Getulio Vargas, Rio de Janeiro, Brazil*

(Received 18 December 2024; accepted 14 July 2025; published 4 August 2025)

Point tomography is an approach to the problem of state estimation, which is arguably the most efficient and simple method for modern high-precision quantum information experiments. In this scenario, the experimenter knows the target state that their device should prepare, except that intrinsic systematic errors will create small discrepancies in the state actually produced. By introducing a kind of informationally complete measurement, dubbed Fisher-symmetric measurements, point tomography determines deviations from the expected state with optimal efficiency. Moreover, the number of outcomes of a measurement saturating the Gill-Massar limit for reconstructing d-dimensional quantum states can be greatly reduced from $\sim 4d-3$ to only $2d-1$ outcomes. Thus, improving the measurement overhead as the dimension increases. Here we demonstrate the experimental viability of point tomography. Using a modern photonic platform constructed with state-of-the-art multicore optical fiber technology, we generate four-dimensional quantum states and implement seven-outcome Fisher-symmetric measurements. Our experimental results exhibit the main feature of point tomography, namely, a precision close to the Gill-Massar limit with a single few-outcome measurement. Specifically, we achieved a precision of $(3.81 \pm 0.05)/N$, while the Gill-Massar limit for $d = 4$ is $3/N$ (N being the ensemble size).

DOI: 10.1103/gpfl-wdgg

I. INTRODUCTION

High-dimensional quantum states (qudits) exhibit important advantages over bidimensional systems for quantum information processing. For instance, qudits can increase sensitivity in quantum metrology [1–3] and efficiency in quantum computing [4–8]. Nonetheless, the benefits of adopting qudit states may be overshadowed by the difficulty in estimating them accurately, impairing our capability to generate, control, and transmit them. This has led to the design of various estimation methods aimed at achieving high estimation precision or reducing the resources required by the estimation process. Modern adaptive quantum tomography methods, for example, rely on interactive algorithms to reach the Gill-Massar limit [9] for some particular quantum states [10–14]. Unfortunately, in general, their efficiencies quickly degrade or the protocol becomes too complex to implement as the dimension of the system increases [15].

Single-setting tomographic methods provide an alternative to adaptive methods [16]. In this approach, a single positive-operator-valued measure (POVM) is used for the state reconstruction. If the recorded statistics of the outcomes of the POVM are sufficient to reconstruct the quantum state, the POVM is said to be informationally complete. The POVM is also said to be globally informationally complete if it can be used to reconstruct any unknown quantum state, in which case the POVM must have at least d^2 elements [16,22] for a d-dimensional system. There have been several theoretical and experimental studies adopting globally informationally complete POVMs [17–21]. Nevertheless, since the scalability of the number of outcomes is demanding, many of the experimental demonstrations actually do not fully implement the required generalized measurement. Instead, they rely on measuring the statistics of each outcome independently, and therefore, the simplicity provided by single-setting tomography is replaced by d^2 different measurements.

A modern take on POVM-based state reconstruction is provided by point tomography [22,23], which finds practical relevance for modern quantum platforms that can achieve high precision in quantum information tasks. Point tomography departs from previous methods by relying not on globally but instead on locally complete POVMs. The kind of measurement used, namely, Fisher-symmetric measurements, is chosen such that the Fisher information is distributed

*Contact author: glima@udec.cl

Published by the American Physical Society under the terms of the Creative Commons Attribution 4.0 International license. Further distribution of this work must maintain attribution to the author(s) and the published article's title, journal citation, and DOI.

uniformly among a set of parameters that uniquely identify quantum states in the neighborhood of an arbitrary target state. Thus, point tomography neatly applies to the situation where the experimentalist has a well-characterized preparation device that emits a state with only small systematic deviations from the target state. Choosing the proper POVM, the method can saturate the Gill-Massar limit. Besides high precision, point tomography has another huge practical advantage. By resorting only to locally complete POVMs, the number of POVM outcomes can be drastically reduced. Thus, improving the measurement overhead as the dimension increases. In the case of pure quantum states, the number of outcomes can be reduced from $\sim 4d-3$ to only $2d-1$ [22,23].

Here, we use state-of-the-art multicore optical fiber technology to demonstrate for the first time the experimental viability of this point tomography method. With this photonic platform, we are able to generate path-encoded four-dimensional quantum states with a high degree of precision [24] and implement high-fidelity genuine seven-outcome POVMs [25]. Our experimental results exhibit the main feature of point tomography, namely, a precision close to the Gill-Massar limit with a single few-outcome Fisher-symmetric measurement. A fit of the experimental data provides an estimation accuracy of $(3.81 \pm 0.05)/N$, while the Gill-Massar limit for $d = 4$ is $3/N$ (N being the ensemble size). This result is even valid for an ensemble as small as $N = 50$. Furthermore, we also experimentally test the method for states in a broader neighborhood. In this case, the estimation precision decreases, as expected, but we see that for small ensembles it is still possible to achieve a precision comparable to the Gill-Massar limit. Our results help pave the way for a broader adoption of point tomography, which resonates well with all modern quantum platforms being developed for high-precision quantum information processing [26,27].

II. METHOD

As discussed above, *a priori* information is used in the construction of Fisher-symmetric measurements. That is, the state $|\psi\rangle$ to be estimated must be in the neighborhood of a given arbitrary fiducial state $|0\rangle$,

$$|\psi\rangle = \frac{1}{A}\left(|0\rangle + \sqrt{\theta}\sum_{j=1}^{3}|j\rangle\right), \tag{1}$$

where A is a normalization constant, $\{|j\rangle\}$ with $j = 1,\ldots,d-1$ is an orthornormal basis, and the coefficient θ is infinitesimal $|\theta|^2 \ll 1$. The quality of the characterization depends on how small this parameter is. Then, the aim of point tomography is to estimate $|\psi\rangle$ with the ultimate precision provided by the Gill-Massar bound, while also maintaining the classical Fisher information matrix uniformly distributed over the target state $|0\rangle$. As has been demonstrated in Ref. [22], all rank-1 POVMs $|\phi^\eta\rangle\langle\phi^\eta|$ ($\eta = 1,\ldots,2d-1$), with $|\phi^\eta\rangle = \sum_{j=0}^{d-1} a_j^\eta |j\rangle$ and a_0^η real, define a Fisher-symmetric measurement if the matrix C, with elements $C_{j,k} = \sum_{\eta=1}^{2d-1} a_j^\eta a_k^\eta$ ($j,k = 1,\ldots,d-1$), has null norm (see the Supplemental Material for details [28]).

Recently, a method to implement high-quality POVMs in a d-dimensional Hilbert space using $D \times D$ modern multiport beam splitters (MBS) was presented [25]. For a photonic qudit, encoded in terms of d spatial optical modes, a rank-1 POVM is realized by connecting these modes to d of the D inputs of the MBS ($D > d$). Thus, by connecting different sets of inputs, there are $D!/[d!(D-d)!]$ different classes of possible POVMs that can be implemented. Exploiting the fact that relative phases can be imprinted between the optical modes before the MBS, the rank-1 POVM elements are proportional to the matrices

$$|\eta_j\rangle = \Phi^\dagger_{k_1\cdots k_d} M_{k_1\cdots k_d}\,|j\rangle\,, \tag{2}$$

where $k_1\cdots k_d$ defines the connected input modes of the MBS, $\Phi_{k_1\cdots k_d}$ is a diagonal matrix defining the phases applied before the MBS, and $M_{k_1\cdots k_d}$ is a $D \times d$ matrix, which is the part of the MBS $D \times D$ unitary matrix acting on the modes $k_1\cdots k_d$.

In this work, we are interested in implementing a Fisher-symmetric seven-outcome measurement onto a four-dimensional fiducial state using the technique of Ref. [25]. In this case, there are 35 different types of POVMs defined by Eq. (2) that could possibly be used in point tomography. For our particular implementation, these measurements are given explicitly in the Supplemental Material [28]. In order to select the best POVM candidate, we minimize the 2-norm of the matrix C for each family of feasible POVMs. We find that even though we cannot implement a Fisher-symmetric measurement exactly, there is a configuration close to a perfect one, where the corresponding matrix C has norm $||C|| \approx 0.63$. Notice that this value is smaller than the average obtained from Haar random POVMs with seven rank-1 elements, given by $||C|| \approx 0.923$ (see Ref. [28] for details). As we demonstrate experimentally next, even in this case point tomography method works quite well.

III. EXPERIMENT

Our experimental setup is depicted in Fig. 1. It has two main stages dedicated for state preparation and POVM implementation. The experiment relies on modern multicore optical fiber (MCF) technologies, which have been developed to meet the increasing demand for bandwidth in optical communication networks [29]. In MCFs, light is transmitted through multiple single-mode cores that are contained within a common cladding. Since the crosstalk between them is depreciable, such core modes can be used to encode d-dimensional photonic quantum systems. Contrary to standard fiber arrays, the cores of multicore fibers lie within the same cladding, ensuring that random phase fluctuations induced by thermal and mechanical stress are strongly suppressed. In a series of independent studies (see Ref. [30] for a comprehensive review), such platform has been shown to achieve high precision in many different quantum information tasks, ranging from high-dimensional quantum communication [31–34], entanglement generation [35–38], to more efficient quantum computing approaches [8].

The purpose of the preparation stage is to generate four-dimensional quantum states. This is accomplished by using the path-encoding strategy for a single-photon propagating over a four-core fiber [24]. The basis states $|i\rangle$, with

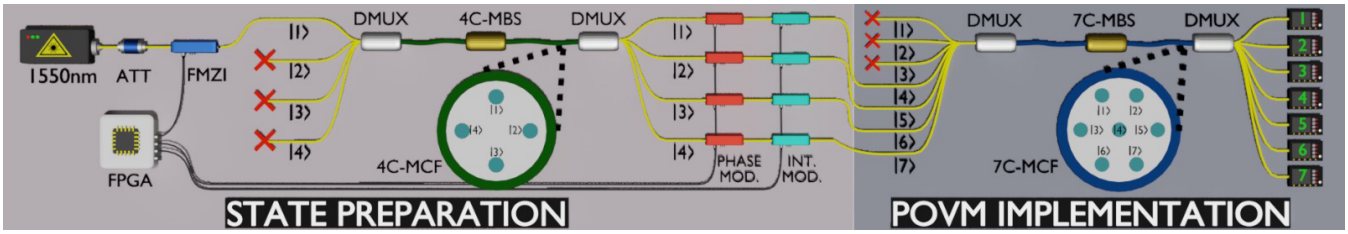


FIG. 1. Experimental setup. In the preparation stage, single-photon states are generated with a CW laser, an attenuator (Att), and a Mach-Zehnder-based intensity modulator (FMZI). The light is distributed from one of the fiber cores to all four of them by a 4C-MBS (four-core multicore beam splitter). The cores are separated into fibers, and the intensity and phase of each one are modulated by phase modulators (PMs) and variable intensity modulators (IMs) to prepare four-dimensional single-photon states. In the measurement stage, the four fibers are fed into a 7C-MBS (seven-core multicore beam splitter) and each of the seven outputs is sent to a single-photon detector (D1 through D7). Since the number of outcomes from the 7C-MBS is greater than 4, the corresponding measurement is a POVM. See the main text for details.

$i = 0, 1, 2, 3$, denote the state of a photon transmitted by the ith core of the MCF. In our setup, a semiconductor telecom continous wave (CW) laser operating at 1546 nm, followed by an attenuator (Att) and an external fiber-pigtailed intensity modulator (IM)- are used to generate weak coherent states comprised of 5-ns-long pulses at a rate of 2 MHz. The IM is controlled by a field programmable gate array unit (FPGA). The mean photon number per pulse generated is adjusted to $\mu = 0.10$. In this case, the contribution of multiphoton events to the recorded statistics is only 0.47% and is, therefore, negligible. The generated single photon is first sent over a single-core fiber of a DMUX, which is a device composed of N single-core fibers connected to a single N-core fiber, where each single-core fiber is mapped to one of the cores of the MCF. The single photon is then transmitted to one of the cores of the 4C-MCF at the end of the DMUX.

This first DMUX is connected to a 4×4 MBS (4C-MBS in Fig. 1). The 4×4 MBSs are manufactured by locally heating a small transverse region of a homogeneous four-core fiber and applying a controlled longitudinal stretching tension. This leads to a tapered fiber where, due to evanescent coupling, photons will jump from one core to the others [24]. The 4C-MBS has a mean fidelity of $F = 0.995 \pm 0.003$ [24] with

$$U_4 = \frac{1}{2}\begin{bmatrix} 1 & 1 & 1 & 1 \\ 1 & 1 & -1 & -1 \\ 1 & -1 & 1 & -1 \\ 1 & -1 & -1 & 1 \end{bmatrix}, \tag{3}$$

while achieving an almost ideal split ratio of 25% (0.248 ± 0.01 [24]). Thus, after the propagation through the MBS, the photon is found in an equally weighted coherent superposition of the $|i\rangle$ basis states. Next, the 4×4 MBS is connected to another DMUX in reverse. Each of the four single-core fibers coming from this DMUX is supplemented with phase and intensity modulators (PMs and IMs, respectively) to control state parameters. While the IM voltages can be set manually, the PM voltages must be constantly adjusted as the optical paths on the single-mode fibers slowly drift. This is accomplished by having the FPGA controlling the PMs with a feedback algorithm based on counts recorded by the single-photon detectors [39]. At this stage of the setup, single-photon states $|\chi\rangle = \sum_{i=0}^{3} \alpha_j e^{i\phi_i} |i\rangle$ can be generated, thus defining the preparation stage for four-dimensional path-encoded states.

The single photons are then sent to the measurement stage through four single-core fibers connected to the third and different DMUX, which now maps seven single-core fibers into a single seven-core fiber. Four of the DMUX's inputs are connected to these fibers, while the other three are not connected to any light source. The DMUX's output is connected to a 7×7 MBS (7C-MBS in Fig. 1) that is followed by another DMUX, which is identical to the third DMUX but in reverse. Finally, the light coming out of each of the seven single-core fibers is detected with InGaAs single-photon detection modules (D1 through D7). The FPGA records the counts of all detectors. To characterize the quality of the interference, we use the visibility, which we define as

$$V = \frac{p_t - \max p_{\neq t}}{p_t + \max p_{\neq t}}, \tag{4}$$

where p_t is the probability of projecting onto a given target state and $\max p_{\neq t}$ is the largest probability of projecting onto one of the three orthogonal states. The average visibility observed is $99.30 \pm 0.02\%$. The combination of DMUXs, MBS, and detectors defines the measurement stage, which realizes a POVM with seven elements acting on the four-dimensional state $|\chi\rangle$. The elements of the POVM are dependent on which of the input fibers are used, as well as the 7×7 matrix describing the MBS. The process tomography of the 7×7 MBS used in our experiment was presented in Ref. [24] and its matrix is given explicitly in the Supplemental Material [28]. The chosen POVM, to study experimentally the method of point tomography, is obtained when the four outputs of the preparation stage are connected to the inputs $i = 4, 5, 6$, and 7 of the measurement stage [28].

IV. RESULTS

We experimentally study the accuracy achievable by the method of point tomography, while considering three different states $|\psi_i\rangle$ [see Eq. (1)], with $\theta_1 = 10^{-2}$, $\theta_2 = 10^{-1}$, and $\theta_3 = 2 \times 10^{-1}$. As θ_i increases, the states $|\psi_i\rangle$ move away from the fiducial state $|0\rangle$ and the efficiency of the estimation process is expected to decrease.

The statistics generated by measuring each state is post-processed by the maximum likelihood estimation technique [40]. The error of the infidelity value experimentally recorded is calculated using Monte Carlo simulations. To model the experimental results, we assume the traditional white noise

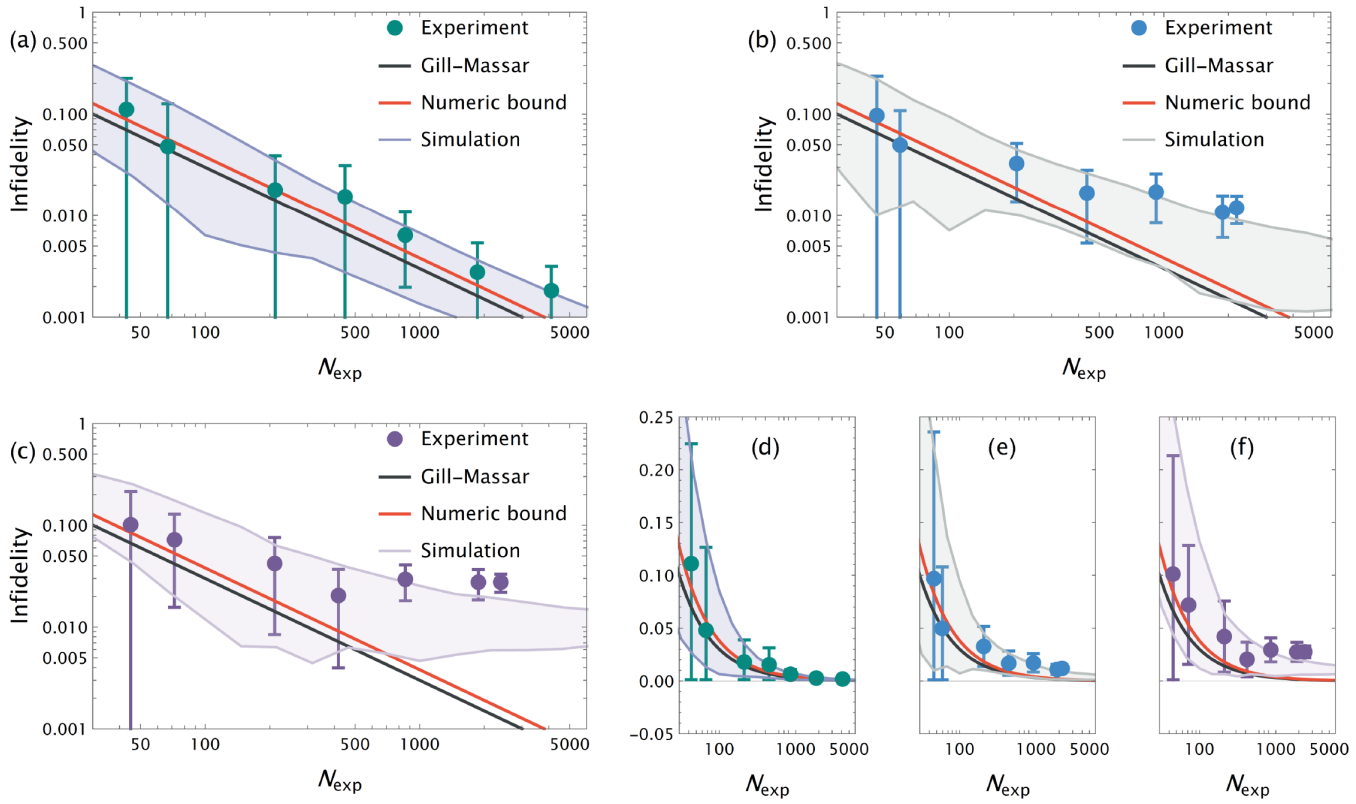


FIG. 2. Experimental results. Insets (a), (b), and (c) are log-log plots for states $|\psi_1\rangle$, $|\psi_2\rangle$, and $|\psi_3\rangle$, respectively, showing the infidelity as a function of sample size. The filled circles indicate the measured infidelity values, while vertical bars indicate one standard deviation for the infidelity values obtained using the Monte Carlo technique. The black solid line corresponds to the Gill-Massar limit for the infidelity given by $3/N$, and the red solid line is the best achievable infidelity for our setup considering the FSM implemented [28]. The shaded area shows the interquartile range generated by our error model. Insets (d), (e), and (f) show the same data as insets (a), (b), and (c), respectively, using a linear-log scale in order to show the typical reduction of the errors due to the increase in sample size.

model. The reason for this is that the low error rate in our experiment is mainly due to detectors' dark counts, which will generate random and perfectly weighted bit-flip errors for all measurement bases. In our model, we consider a noisy state given by $\rho = \lambda|\psi\rangle\langle\psi| + (1-\lambda)I/d$. Using the experimentally obtained value 0.9930 ± 0.0002 for the visibility defined in Eq. (4) and considering dimension $d = 4$, we have $\lambda = V/(2-V) \approx 0.987$. This state has associated with it a noisy probability distribution, p^η, given in terms of the elements of the FSM POVM $|\phi^\eta\rangle\langle\phi^\eta|$. Using these probabilities, we generate 10^3 Monte Carlo simulated experiments resorting to a random multinomial distribution. We repeat this procedure for different ensemble sizes. For each simulated experiment, we construct an estimator $|\chi_j\rangle$. We then compute the infidelity of each estimator, $I_j = 1 - |\langle\chi_j|\psi\rangle|$, resulting in a set $\{I_j\}$.

The experimental results are presented in Figs. 2(a)–2(c) for states $|\psi_1\rangle$, $|\psi_2\rangle$, and $|\psi_3\rangle$, respectively, which show the infidelity as a function of the ensemble size N (both axes in logarithmic scale). The filled circles indicate the measured infidelity values, while vertical bars indicate one standard deviation for the infidelity values obtained using the Monte Carlo technique. The black solid line corresponds to the Gill-Massar limit for the infidelity given by $3/N$, and the red solid line is the best achievable infidelity for our setup, considering the FSM implemented [28], corresponding to $(3.81 \pm 0.05)/N$. It was obtained numerically by calculating the Fisher information matrices for the POVM that was used, when applied to an ideal state without any white noise. The shaded area shows the interquartile range generated by our error model.

Figure 2(a) shows the case where we estimate state $|\psi_1\rangle$, which has the largest fidelity with respect to the fiducial state $|0\rangle$. The infidelity exhibits values very close to both the Gill-Massar bound and those of the white noise model in the inspected interval of ensemble size. This shows that the implemented POVM is able to estimate the state $|\psi_1\rangle$ with high precision following a trend similar to the Gill-Massar limit. Specifically, a fit of the experimental results related with state $|\psi_1\rangle$ leads to a infidelity behavior that decreases as a function of the ensemble size N according to $(4.33 \pm 0.42)/N$, which is quite close to the limit imposed by our POVM. Even the highest infidelity values for smaller ensembles do not differ significantly from this bound. Figures 2(b) and 2(c) show results for larger imposed systematic errors. In these two cases and for small ensemble sizes, the experimental setup provides infidelity values still close to the Gill-Massar limit, giving $(3.41 \pm 1.00)/N$ for state $|\psi_2\rangle$ and $(4.44 \pm 0.85)/N$ for state $|\psi_3\rangle$, where we fit only the first four points (up to around $N = 500$), in the regions in which the data show a linear trend. As the size of the ensemble increases, the infidelity values are higher than in the case of state $|\psi_1\rangle$ and clearly differ from the lower Gill-Massar bound. Moreover, for the largest

ensemble sizes, the infidelity values start to plateau. This is an experimental indication of the limits of the neighborhood that may be accurately considered in point tomography, as well as an indication that random errors dominate over the effects of finite statistics for distant states. Finally, note that even though the infidelities for the estimation of $|\psi_2\rangle$ and $|\psi_3\rangle$ follow the general behavior of the white noise model (gray shaded region), systematically our points deviate from this model, when a larger number of measurement events are considered. We believe this may be caused by small fluctuations in the attenuation provided by the intensity modulators, which would generate slightly higher theta values for the last measurement events recorded. Figures 2(d)–2(f) are used only to show the error bars out of the logarithmic scale for each case considered, where one can see the typical reduction of the errors due to the increase in sample size.

V. CONCLUSION

We have successfully demonstrated the viability of point tomography, a state estimation technique that has practical relevance for modern high-precision quantum information processing. Specifically, assuming that an arbitrary target state can be prepared with high accuracy by the experimentalist, the method offers an estimation efficiency that saturates the Gill-Massar limit, while requiring the implementation of a simpler POVM whose number of outcomes can be greatly reduced from the traditional value of $\sim 4d - 3$ to only $2d - 1$, making POVM-based tomography for higher dimensions ($d \geqslant 2$) much more viable. In our work, we use state-of-the-art multicore optical fiber technology to efficiently generate four-dimensional quantum states and to implement measurements in the form of a seven-outcome generalized measurement. Notably, in our work the Fisher-symmetric POVM is implemented in a plug-and-play architecture, realized by a single multiport beam splitter [25]. However, point tomography can be implemented using any platform capable of realizing Fisher-symmetric POVMs. Since by Neumark's theorem a POVM can be achieved via a projective measurement in a larger Hilbert space, point tomography should be a useful tool in most quantum information processing devices and scenarios where a fiducial state is expected, especially due to the reduction in the measurements.

Our experimental investigation clearly demonstrates the viability of point tomography in higher-dimensional systems for several states close to the fiducial one. In the high-precision regime, we observe a precision trend close to the Gill-Massar limit even though the POVM performed is not exactly a Fisher-symmetric measurement. In lower-precision regimes, we show that the method can still be relevant. For small ensemble sizes where statistical errors dominate, the average infidelities are still close to the Gill-Massar bound and show a linear decrease in the log-log plot as the ensemble size increases. The robustness of the method demonstrated in our work paves the way for a broader adoption of point tomography in all modern quantum platforms developed for high-precision quantum information.

ACKNOWLEDGMENTS

This work was supported by Fondo Nacional de Desarrollo Científico y Tecnológico (FONDECYT) Grants No. 1240746, No. 1231940, No. 1240843, and No. 3200820, and by ANID—Millennium Science Initiative Program—ICN17_012. L.P. was supported by the Government of Spain (Severo Ochoa CEX2019-000910-S, FUNQIP, Quantum in Spain, and European Union NextGenerationEU PRTR-C17.I1), Fundació Cellex, Fundació Mir-Puig, and Generalitat de Catalunya (CERCA program). K.S. was supported by the UCO 1866. M.M. was supported by ANID-PFCHA/DOCTORADO-NACIONAL/2019-21190958.

DATA AVAILABILITY

The data that support the findings of this article are not publicly available upon publication because it is not technically feasible and/or the cost of preparing, depositing, and hosting the data would be prohibitive within the terms of this research project. The data are available from the authors upon reasonable request.

[1] S. Lloyd, Enhanced sensitivity of photodetection via quantum illumination, Science **321**, 1463 (2008).

[2] M. Szczykulska, T. Baumgratz, and A. Datta, Multi-parameter quantum metrology, Adv. Phys.: X **1**, 621 (2016).

[3] F. Albarelli, M. Barbieri, M. G. Genoni, and I. Gianani, A perspective on multiparameter quantum metrology: From theoretical tools to applications in quantum imaging, Phys. Lett. A **384**, 126311 (2020).

[4] B. Lanyon, M. Barbieri, M. Almeida, T. Jennewein, T. C. Ralph, K. J. Resch, G. J. Pryde, J. L. O'Brien, A. Gilchrist, and A. G. White, Simplifying quantum logic using higher-dimensional Hilbert spaces, Nat. Phys. **5**, 134 (2009).

[5] A. Bocharov, M. Roetteler, and K. M. Svore, Factoring with qutrits: Shor's algorithm on ternary and metaplectic quantum architectures, Phys. Rev. A **96**, 012306 (2017).

[6] A. Babazadeh, M. Erhard, F. Wang, M. Malik, R. Nouroozi, M. Krenn, and A. Zeilinger, High-dimensional single-photon quantum gates: Concepts and experiments, Phys. Rev. Lett. **119**, 180510 (2017).

[7] S. Muralidharan, C.-L. Zou, L. Li, J. Wen, and L. Jiang, Overcoming erasure errors with multilevel systems, New J. Phys. **19**, 013026 (2017).

[8] M. Taddei *et al.*, Computational advantage from the quantum superposition of multiple temporal orders of photonic gates, PRX Quantum **2**, 010320 (2021).

[9] R. D. Gill and S. Massar, State estimation for large ensembles, Phys. Rev. A **61**, 042312 (2000).

[10] C. Ferrie, Self-guided quantum tomography, Phys. Rev. Lett. **113**, 190404 (2014).

[11] D. H. Mahler, L. A. Rozema, A. Darabi, C. Ferrie, R. Blume-Kohout, and A. M. Steinberg, Adaptive quantum state tomography improves accuracy quadratically, Phys. Rev. Lett. **111**, 183601 (2013).

[12] S. S. Straupe, Adaptive quantum tomography, JETP Lett. **104**, 510 (2016).

[13] G. I. Struchalin, E. V. Kovlakov, S. S. Straupe, and S. P. Kulik, Adaptive quantum tomography of high-dimensional bipartite systems, Phys. Rev. A **98**, 032330 (2018).
[14] F. Huszár and N. M. T. Houlsby, Adaptive Bayesian quantum tomography, Phys. Rev. A **85**, 052120 (2012).
[15] L. Pereira, L. Zambrano, J. Cortés-Vega, S. Niklitschek, and A. Delgado, Adaptive quantum tomography in high dimensions, Phys. Rev. A **98**, 012339 (2018).
[16] J. M. Renes, R. Blume-Kohout, A. J. Scott, and C. M. Caves, Symmetric informationally complete quantum measurements, J. Math. Phys. **45**, 2171 (2004).
[17] D. M. Appleby, H. B. Dang, and C. A. Fuchs, Symmetric informationally-complete quantum states as analogues to orthonormal bases and minimum-uncertainty states, Entropy **16**, 1484 (2014).
[18] J. Rehacek, B.-G. Englert, and D. Kaszlikowski, Minimal qubit tomography, Phys. Rev. A **70**, 052321 (2004).
[19] W. M. Pimenta *et al.*, Minimal state tomography of spatial qubits using a spatial light modulator, Opt. Express **18**, 24423 (2010).
[20] N. Bent, H. Qassim, A. A. Tahir, D. Sych, G. Leuchs, L. L. Sánchez-Soto, E. Karimi, and R. W. Boyd, Experimental realization of quantum tomography of photonic qudits via symmetric informationally complete positive operator-valued measures, Phys. Rev. X **5**, 041006 (2015).
[21] R. Stricker, M. Meth, L. Postler, C. Edmunds, C. Ferrie, R. Blatt, P. Schindler, Th. Monz, R. Kueng, and M. Ringbauer, Experimental single-setting quantum state tomography, PRX Quantum **3**, 040310 (2022).
[22] N. Li, C. Ferrie, J. A. Gross, A. Kalev, and C. M. Caves, Fisher-symmetric informationally complete measurements for pure states, Phys. Rev. Lett. **116**, 180402 (2016).
[23] H. Zhu and M. Hayashi, Universally Fisher-symmetric informationally complete measurements, Phys. Rev. Lett. **120**, 030404 (2018).
[24] J. Cariñe, G. Cañas, P. Skrzypczyk, I. Šupić, N. Guerrero, T. Garcia, L. Pereira, M. A. S. Prosser, G. B. Xavier, A. Delgado, S. P. Walborn, D. Cavalcanti, and G. Lima, Multi-core fiber integrated multi-port beam splitters for quantum information processing, Optica **7**, 542 (2020).
[25] D. Martínez, E. S. Gómez, J. Cariñe, L. Pereira, A. Delgado, S. P. Walborn, A. Tavakoli, and G. Lima, Certification of a non-projective qudit measurement using multiport beamsplitters, Nat. Phys. **19**, 190 (2023).
[26] S. Pirandola *et al.*, Advances in quantum cryptography, Adv. Opt. Photonics **12**, 1012 (2020).
[27] A. K. Fedorov, N. Gisin, S. M. Beloussov, A. I. Lvovsky, Quantum computing at the quantum advantage threshold: A down-to-business review, arXiv:2203.17181.
[28] See Supplemental Material at http://link.aps.org/supplemental/10.1103/gpfl-wdgg for futher details about the theory and components employed in the experiment.
[29] D. Richardson, J. Fini, and L. Nelson, Space-division multiplexing in optical fibres, Nat. Photon. **7**, 354 (2013).
[30] G. B. Xavier and G. Lima, Quantum information processing with space-division multiplexing optical fibres, Commun. Phys. **3**, 9 (2020).
[31] Y. Ding, D. Bacco, K. Dalgaard, X. Cai, X. Zhou, K. Rottwitt, L. K. Oxenløwe, High-dimensional quantum key distribution based on multicore fiber using silicon photonic integrated circuits, npj Quantum Inf. **3**, 25 (2017).
[32] G. Cañas, N. Vera, J. Cariñe, P. Gonález, J. Cardenas, P. W. R. Connolly, A. Przysiezna, E. S. Gómez, M. Figueroa, G. Vallone, P. Villoresi, T. Ferreira da Silva, G. B. Xavier, and G. Lima, High-dimensional decoy-state quantum key distribution over multicore telecommunication fibers, Phys. Rev. A **96**, 022317 (2017).
[33] S. Sarmiento, S. Etcheverry, J. Aldama, I. H. López, L. T. Vidarte, G. B. Xavier, D. A. Nolan, J. S. Stone, M. J. Li, D. Loeber, and V. Pruneri, Continuous-variable quantum key distribution over a 15 km multi-core fiber, New J. Phys. **24**, 063011 (2022).
[34] M. Zahidy, D. Ribezzo, C. De Lazzari *et al.*, Practical high-dimensional quantum key distribution protocol over deployed multicore fiber, Nat. Commun. **15**, 1651 (2024).
[35] H. J. Lee, S.-K. Choi, and H. S. Park, Experimental demonstration of four-dimensional photonic spatial entanglement between multi-core optical fibres, Sci. Rep. **7**, 4302 (2017).
[36] H. J. Lee and H. S. Park, Generation and measurement of arbitrary four-dimensional spatial entanglement between photons in multicore fibers, Photonics Res. **7**, 19 (2019).
[37] E. A. Ortega *et al.*, Experimental space-division multiplexed polarization-entanglement distribution through 12 paths of a multicore fiber, PRX Quantum **2**, 040356 (2021).
[38] E. S. Gómez, S. Gómez, I. Machuca, A. Cabello, S. Pádua, S. P. Walborn, and G. Lima, Multidimensional entanglement generation with multicore optical fibers, Phys. Rev. Appl. **15**, 034024 (2021).
[39] H. Abarzúa *et al.*, Adaptive-step perturb-and-observe algorithm for multidimensional phase noise stabilization in fiber-based multi-arm Mach-Zehnder interferometers, Algorithms **17**, 534 (2024).
[40] J. Shang, Z. Zhang, and H. K. Ng, Superfast maximum-likelihood reconstruction for quantum tomography, Phys. Rev. A **95**, 062336 (2017).